

Experimental and Theoretical Charge Density Analysis of Polymorphic Structures: The Case of Coumarin 314 Dye

Parthapratim Munshi,[†] Christian Jelsch,^{*,†} Venkatesha R. Hathwar,[‡] and Tayur N. Guru Row[‡]

[†]Laboratoire de Crystallographie, Résonance Magnétique et Modélisations, CRM2, CNRS, UMR 7036, Nancy Université, Faculté des Sciences et Techniques, BP 70239, 54506 Vandoeuvre-lès-Nancy CEDEX, France, and [‡]Solid State and Structural Chemistry Unit, Indian Institute of Science, Bangalore-560012, India

Received June 10, 2009; Revised Manuscript Received February 5, 2010

ABSTRACT: Experimental charge density distributions in two known conformational polymorphs (orange and yellow) of coumarin 314 dye are analyzed based on multipole modeling of X-ray diffraction data collected at 100 K. The experimental results are compared with the charge densities derived from multipole modeling of theoretical structure factors obtained from periodic quantum calculation with density functional theory (DFT) method and B3LYP/6-31G(d,p) level of theory. The presence of disorder at the carbonyl oxygen atom of ethoxycarbonyl group in the yellow form, which was not identified earlier, is addressed here. The investigation of intermolecular interactions, based on Hirshfeld surface analysis and topological properties via quantum theory of atoms in molecule and total electrostatic interaction energies, revealed significant differences between the polymorphs. The differences of electrostatic nature in these two polymorphic forms were unveiled via construction of three-dimensional deformation electrostatic potential maps plotted over the molecular surfaces. The lattice energies evaluated from ab initio calculations on the two polymorphic forms indicate that the yellow form is likely to be the most favorable thermodynamically. The dipole moments derived from experimental and theoretical charge densities and also from Lorentz tensor approach are compared with the single-molecule dipole moments. In each case, the differences of dipole moments between the polymorphs are identified.

Introduction

Coumarins and the substituted coumarin derivatives have been extensively studied as they find useful applications in the dye industry¹ and in the area of laser dyes.² Coumarins are also used in several areas of synthetic chemistry, medicinal chemistry, and photochemistry. The formation of a [2 + 2] cycloaddition product upon irradiation of coumarin and its derivatives has contributed immensely to the area of solid-state photochemistry.³ These compounds show state-dependent variation in the static dipole moment. A wide variety of pharmacological activities, such as antiviral⁴ and antimicrobial activity,⁵ are exhibited by coumarin derivatives, and they form the basic building block in the well-known antibiotic novobiocin.⁶ Coumarin dyes such as coumarin 138,⁷ coumarin 152,⁸ coumarin 153,⁹ and coumarin 314^{10,11} are found to exist in two different crystalline forms. The phenomenon, existence of a crystal structure in more than one crystalline form, is known as polymorphism.¹² Further, 4-styrylcoumarin,¹³ 3-acetylcoumarin,¹⁴ and fluoro derivative of coumarin¹⁵ also display polymorphism. In recent years, the occurrence of polymorphism in molecular crystals has received considerable attention, especially from the *drug design* and *crystal engineering* viewpoint.^{12,16,17}

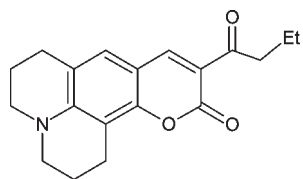
Charge density analysis is now an established subfield of crystallography. Although there are numerous reports of polymorphic structures in the literature,¹² the number of charge density studies carried out on such systems is very scarce.^{14b,18,19} To our knowledge, there is just one example of

an organic polymorph (3-acetylcoumarin) studied via both experimental and theoretical charge density analyses by some of us.^{14b} As pointed out by Overgaard and Hibbs,¹⁸ studies of this kind are potentially highly rewarding. The advantage of a charge density approach is clear from the Hohenberg–Kohn theorem,²⁰ which states that all ground-state properties are a unique function of the charge density. To add some more contributions in this field of charge density, we have performed quantitative analyses of experimental and theoretical charge density distributions in two known conformational polymorphs of coumarin 314 dye (Scheme 1). This allows us to have a better understanding of the charge density features associated with the polymorphic structures in general.

The surface features, or topology, of the charge density distribution obtained from experimental or theoretical methods can be analyzed via Bader's quantum theory of atoms in molecules (AIM).²¹ This approach provides a pathway for comparison of the experimental electron density with the theoretically derived density in terms of the topological properties of the charge density $\rho(\mathbf{r})$. The topology of a scalar field, such as $\rho(\mathbf{r})$, which is a physical quantity, can conveniently be summarized in terms of critical points (CP), where the first derivatives of $\rho(\mathbf{r})$ vanish, $\nabla\rho(\mathbf{r}) = 0$, indicating the position of extrema (maxima, minima, or saddle points). In general, the theory of AIM provides a methodology for the identification of a bond between any two atoms in a molecule in terms of CPs, called bond critical points (BCP). An important function of $\rho(\mathbf{r})$ is its second derivative, the Laplacian $\nabla^2\rho(\mathbf{r})$, which is a scalar quantity and is defined as the sum of the principal curvatures ($\lambda_1 + \lambda_2 + \lambda_3$). It is a representation of the chemical features of the molecule. The physical significance of the Laplacian is that it represents areas of local charge

*To whom correspondence should be addressed. Telephone: +33 (0)3 83 68 48 99. Fax: +33 (0)3 83 40 64 92. E-mail: christian.jelsch@crm2.uhp-nancy.fr.

Scheme 1. Chemical Diagram of Coumarin 314



concentration and depletion. If $\nabla^2\rho(\mathbf{r}) < 0$, the density is locally concentrated resulting in shared interactions, while in the case of $\nabla^2\rho(\mathbf{r}) > 0$, the electron density is depleted representing closed-shell interactions. The length of the line of highest electron density linking any two atoms is referred to as the “bond path”, R_{ij} , which need not be the same as the interatomic vector, d . The electron densities, the Laplacian values, the bond paths, the curvatures, and the bond ellipticities (ϵ) together represent the topology of the charge density distribution in a given molecule. Having derived the electron densities $\rho(\mathbf{r})$ and its Laplacian $\nabla^2\rho(\mathbf{r})$, it is possible to relate these quantities to the local electronic kinetic energy density $G(\mathbf{r}_{CP})$ and hence the local potential energy density $V(\mathbf{r}_{CP})$.²²

Experimental and Theoretical Section

Crystallization and Data Collection. All the crystallization experiments were performed at room temperature and in the dark by slow evaporation of solvents. The title compound was purchased as fine powder from Aldrich. The crystallization of coumarin 314 from a mixture of chloroform and ethanol, as described by Yip et al.,¹⁰ resulted in several yellow-colored crystals with “block” type morphology. The cell-checking experiments on these yellow crystals revealed that these are of the original known form, the yellow form.¹⁰ Several attempts were made with the coumarin 314 from Aldrich to grow the crystals of the known orange form in ethanol solution as reported earlier,¹¹ but every time very small or flat crystals of the yellow form appeared. Similar crystals were found even with different solvents such as acetone, ethyl acetate, ether, etc. Later, the title compound was purchased from Acros, which was actually made of orange color crystals. The recrystallization of this compound from an ethanol solution resulted again in block-type crystals, which are of the second known crystal form, the orange form. Interestingly, the recrystallization of this compound from Acros, in mixtures of chloroform and ethanol, always led to the orange crystal form.

Crystals of size ~ 0.3 mm were selected and cooled to 100(3) K with a nitrogen vapor open flow stream device (Oxford Cryosystems 600 series). The crystals were exposed to Mo $K\alpha$ radiation and the X-ray diffraction intensities were measured using a Nonius Kappa CCD diffractometer. Data collections were monitored using the program COLLECT.²³ The crystal-to-detector distance was fixed at 36 mm for the orange form and at 40 mm for the yellow form. In total, four batches of data were collected for each crystal form. For the orange form, the detector positions were set at $2\theta = -13^\circ, 3^\circ, 40^\circ$, and 60° , while for the yellow form the positions were at $2\theta = -15^\circ, 2^\circ, 40^\circ$, and 54° . In both cases, the exposure times were set to 30, 60, and 180 s for the two low, the medium, and the high resolution sets of frames, respectively. The scan angle per frame was $\Delta\omega = 1^\circ$. A total of 2171 and 1786 frames were collected over a period of 3 days for the orange and the yellow forms, respectively. The diffraction data collection statistics are summarized in Table 1.

Data Reduction. The integration of intensities was performed using the software DENZO.²⁴ The refinement of the final unit cell parameters based on all the frames collected and the scaling of the frames were performed using SCALEPACK.²⁴ The reflection measurements were merged and the empirical absorption corrections were applied using SORTAV.²⁵ For the orange form, the minimum and maximum transmission factors are 0.854 and

Table 1. Summary of Crystallographic Data

crystal form	orange	yellow
chemical formula	$C_{18}H_{19}O_4N_1$	$C_{18}H_{19}O_4N_1$
molecular density	1.409	1.404
a, b, c (Å)	12.163(2), 11.887(1), 10.224(1)	8.388(1), 14.867(2), 11.919(1)
β (°)	92.38(1)	94.43(1)
V (Å ³)	1476.9(2)	1481.9(2)
space group; Z	$P2_1/n$; 4	$P2_1/n$; 4
$\sin \theta_{\max}/\lambda$ (Å ⁻¹)	1.10	1.03
no. measured reflections	156 578	129 400
no. unique reflections	16 036	13 239
$R_{\text{merge}}(I)$	0.0457	0.0577
Spherical-atom refinement		
GOF (F^2)	0.94	0.88
R_1 ; wR_2 (all data)	0.0492; 0.0967	0.0676; 0.1090
N_{ref}^a ($I > 2\sigma(I)$)	11 954	8316
R_1 ; wR_2 ($I > 2\sigma(I)$)	0.0357; 0.0917	0.0418; 0.1040
Multipole refinement		
GOF (F)	0.84	0.85
N_{ref} ($I > 0\sigma(I)$)	15 398	12 274
R_1 ; wR_2 ($I > 0\sigma(I)$)	0.0340; 0.0492	0.0488; 0.0659
N_{ref} ($I > 2\sigma(I)$)	11 954	8316
R_1 ; wR_2 ($I > 2\sigma(I)$)	0.0231; 0.0475	0.0301; 0.0638
N_{ref} ($I > 3\sigma(I)$)	10 942	7197
R_1 ; wR_2 ($I > 3\sigma(I)$)	0.0209; 0.0462	0.0272; 0.0623

^a N_{ref} : number of reflections used for the refinement

0.871, respectively, and for the yellow form the corresponding values are 0.814 and 0.821. For the orange form, a higher resolution (0.46 Å) of diffraction data was achieved with an average redundancy of 9.7, whereas for the yellow form resolution was slightly lower (0.48 Å) and the average redundancy was 9.8. The relevant details of data reduction for both crystal forms are given in Table 1.

Crystallographic Modeling. Experimental. The structures were solved using SIR94²⁶ and refined in the spherical-atom approximation (based on F^2) using SHELXL97²⁷ included in the package WinGX.²⁸ The charge density modeling and refinement was performed with MoPro²⁹ using Hansen & Coppens multipole formalism.³⁰ It allows describing the atomic electron density as a superposition of pseudoatoms as follows:

$$\rho_{\text{atom}}(\mathbf{r}) = \rho_{\text{core}}(r) + P_{\text{val}}\kappa^3\rho_{\text{val}}(\kappa r) + \sum_{l=0}^{l_{\text{max}}} \kappa^l R_l(\kappa' r) \sum_{m=0}^l P_{lm} \pm y_{lm} \pm (\theta, \varphi)$$

where ρ_{core} and ρ_{val} represent the spherical core and valence unitary electron density, respectively. P_{val} is the valence population parameter and gives an estimation of the net atomic charge $q = N_{\text{val}} - P_{\text{val}}$, where N_{val} is the number of valence electrons. y_{lm} represent multipolar spherical harmonic functions of order l in real form, R_{nl} are Slater type radial functions, and P_{lm} are the multipolar populations. The coefficients κ and κ' describe the contraction–expansion for the spherical and multipolar valence densities, respectively. For the structure factor computations, the form factor for the hydrogen atoms was taken from Stewart et al.,³¹ the form factors for non-hydrogen atoms were calculated from Clementi & Raimondi,³² and wave functions and the real and imaginary dispersion corrections to the form factors were from Kissel et al.³³ Atomic displacement parameters of hydrogen atoms are obtained using the recently described SHADE2 approach.³⁴

Theoretical. Periodic quantum calculations using CRYSTAL06³⁵ were performed at the crystal geometry observed experimentally, and, using these as starting geometries, optimizations were performed with density functional theory (DFT) method at the B3LYP/6-31G(d,p) level of theory. Because of the presence of disorder at one of the atom sites of yellow form (see Results and Discussion) and thus the distorted geometry, it was noticed that the periodic quantum calculation based on the experimental crystal geometry was producing inaccurate theoretical electron densities for yellow form. Therefore, the periodic calculations were performed based on the optimized geometries. For consistency and also for a better comparison, the same approach was

followed for the orange form as well. The thresholds for numerical accuracy and convergence criteria used in CRYSTAL06 were the same as in previous studies.³⁶ Upon convergence on energy ($\sim 10^{-6}$), the periodic wave functions based on optimized geometries were obtained, and the option XFAC was used to generate the theoretical structure factors at the same resolutions as observed from the experiments.

Multipole Refinement. Experimental. The multipolar nonspherical atom refinement was carried out with the full-matrix least-squares program *MoPro*.²⁹ The function minimized was $\sum w(|F_o| - K|F_c|)^2$, for all the reflections with $I/\sigma(I) > 0$. Initially, the scale factor was refined against the whole resolution range of diffraction data. The positional and anisotropic thermal displacement parameters of the non-hydrogen atoms were refined against the reflections with $\sin \theta/\lambda > 0.7 \text{ \AA}^{-1}$. The lower resolution ($\sin \theta/\lambda < 0.7 \text{ \AA}^{-1}$) reflections were used to refine the positional parameters of the hydrogen atoms. The hydrogen-carbon bond lengths were restrained with an allowed standard deviation of 0.002 Å; the targets for $\text{Csp}^2\text{-H}$, $>\text{CH}_2$ and $-\text{CH}_3$ were set to the values obtained from the calculations based on optimized geometries. The optimized bond lengths for $\text{Csp}^2\text{-H}$ and $>\text{CH}_2$ were found to be very similar to the reported average neutron diffraction values.³⁷ However, for the $-\text{CH}_3$ group, the optimized C-H bond lengths were systematically higher ($\sim 1.092 \text{ \AA}$) than the average neutron diffraction values (1.059 \AA) and were similar to that of $>\text{CH}_2$ values (1.092 \AA). For non-hydrogen atoms, the scale, positional and thermal displacement parameters, P_{val} , P_{lm} , κ , and κ' were allowed to refine in a stepwise manner, until the convergence was reached. The multipole expansion was truncated at the hexadecapole level for oxygen and nitrogen atoms and at the octupole level for carbon atoms. Appropriate local site symmetry constraints were imposed on the multipole populations of all the non-hydrogen atoms. Chemically equivalent atoms were constrained to have the same set of κ and κ' . For hydrogen atoms, the anisotropic thermal displacement parameters were fixed to the values obtained from SHADE2 analysis and only bond directed dipole (d_z) and quadrupole (q_{3z^2-1}) components were allowed to refine. Chemically equivalent hydrogen atoms were restrained (with standard deviation of 0.01) to refine with similar values of valence and multipole populations. Three sets of κ and κ' were attributed to the hydrogen atoms, depending on their chemical type, $\text{Csp}^2\text{-H}$, $>\text{CH}_2$, and $-\text{CH}_3$. The κ and κ' values of all atoms were restrained (with standard deviation of 0.002) to the values obtained from the multipole model fitted to the theoretical structure factors, which is detailed in the following section. The advantage of this approach has been discussed elsewhere.³⁸ The same multipole refinement strategy was applied for both the polymorphic forms. However, due to the presence of disorder at the atom site O20 of the yellow form, it was not feasible to refine the charge densities of this atom while the neighboring atom O21, the ester oxygen atom of the ethoxycarbonyl group was also affected. Initially, an effort was made to perform the multipole refinement of these atoms with X-ray diffraction data. However, it led to an unstable model with non-realistic deformation electron densities. Modeling of these atoms using Gram-Charlier expansion even up to fourth-order did not improve the results. Therefore, the multipoles and kappa parameters of the disorder atoms O20A and O20B and of atom O21 were transferred from the theoretical multipole model of the yellow form. It has been realized that the multipole modeling of disordered structure is a challenging problem in high resolution experimental charge density studies.³⁹

Theoretical. During the multipole refinement based on the amplitude of the theoretical structure factors ($|F|$) and with unit sigma on $|F|$, the atomic positions were held fixed to the values obtained from the geometry optimization. To consider a static model, the thermal displacement parameters were set to zero. To allow comparison with experimental results, the same multipoles, as those refined with the X-ray diffraction data, were allowed to refine here for all the atoms. Exactly the same constraints, as those applied in case of experimental multipole model, were imposed here too. However, no restraints were applied on any parameters.

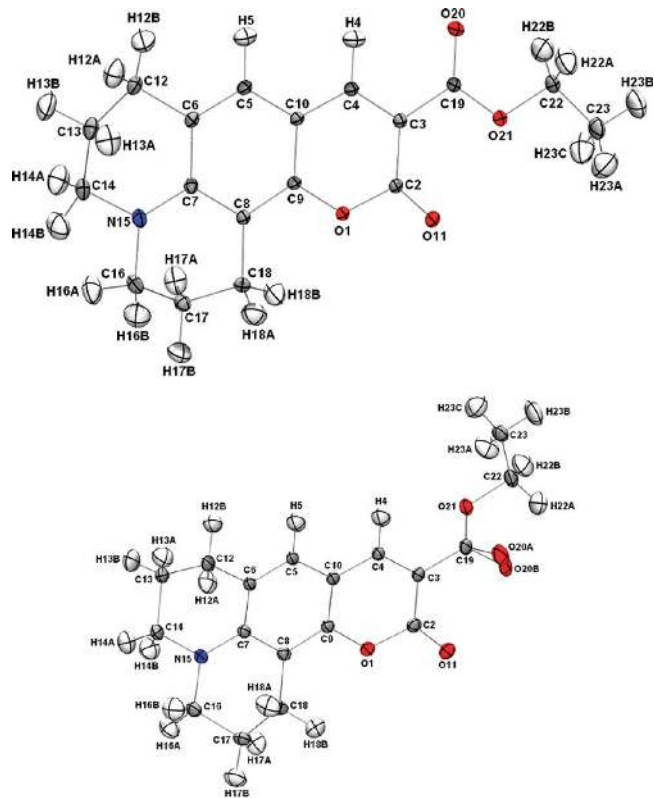


Figure 1. ORTEP diagrams of coumarin 314 at 100 K with 50% ellipsoid probability. The diagrams are generated using ORTEP-III⁴⁰ and POV-Ray.⁴¹

Results and Discussion

Crystal Structures. The crystallographic details and the parameters from multipolar refinement of single crystal X-ray diffraction data for the orange and the yellow forms are listed in Table 1. Both forms crystallize in monoclinic centrosymmetric space group $P2_1/n$ with $Z = 4$. The ORTEP diagram along with the atom labeling of the molecules in the respective forms are displayed in Figure 1. The detailed discussion on geometrical analyses of the yellow¹⁰ and the orange¹¹ forms based on X-ray diffraction data collected at room temperature are already reported in the literature. Although the report on the yellow form points out the higher thermal parameters of atom O20, no disorder was considered for this atom. Interestingly, the present structure determined at 100 K is found to have disorder at atom site O20, and it has two positions with occupancies of 77% (O20A) and 23% (O20B) (Figure 1). On the other hand, the orange form at room temperature is shown to have disorder at atom site C13 (labeled as C16A and C16B in earlier report¹¹), but our present study at 100 K does not display such disorder. For the yellow form, the geometry with highest occupied position of atom O20 (O20A, 77%) was used as a starting geometry for the optimization calculation, and the relevant discussions in the following are also based on this atom, O20A. It is to be noted that the ethoxycarbonyl group in these two polymorphic forms has two distinct conformations, and hence the two crystal forms are conformational polymorphs (Figure 2).

The molecular packing arrangements shown in Figure 3 clearly highlight the distinct orientation of the molecules in the crystals of the two polymorphic forms. However, in both forms, the molecules pack in an antiparallel fashion with

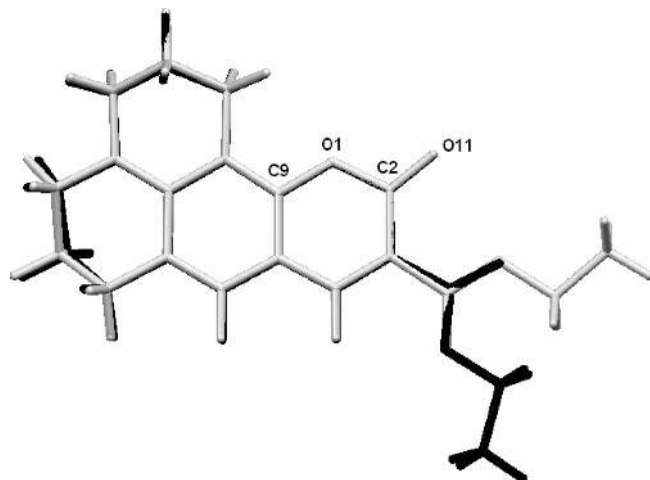


Figure 2. Overlay of polymorphs of coumarin 314 showing the differences in molecular geometry and conformation, the orange form in light gray color and the yellow form in black color. The rotation center is at atom O1 and the molecules are viewed perpendicular to the O1–C2 bond. The diagram is generated using Mercury.⁴²

different orientations. The geometrical analysis via PARST⁴³ revealed that the interplanar distance between the coumarin moieties are 3.5562(4) Å in the orange form and 3.6581(3) Å in the yellow form.

A quite different set of intermolecular contacts were noticed in these two polymorphs and the Hirshfeld surface analysis⁴⁴ was performed with CrystalExplorer⁴⁵ to quantify all of these contacts. The details of the Hirshfeld surface approach for the quantification of intermolecular contacts⁴⁶ and to compare polymorphic forms⁴⁷ have been discussed in their recent articles from Spackman's group. The relative contributions to the Hirshfeld surface areas due to H···H, O···H, C···H and "other" (C···C, O···C, C···N, O···O, O···N, N···N, and N···H) intermolecular contacts are illustrated in Figure 4 for both polymorphs. For the yellow form, the hypothetical "ordered" structure (i.e., atom O20A with 100% occupancy) was considered to construct the entries in the chart in Figure 4. The pictorial representation of the quantitative analysis of intermolecular contacts clearly shows that the two polymorphic forms have similar

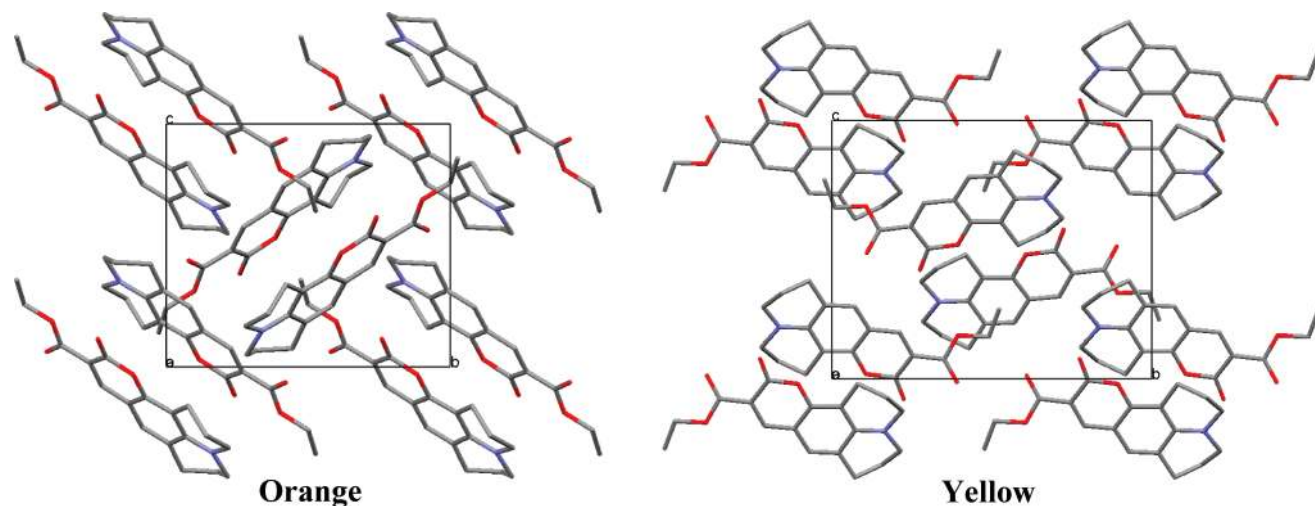


Figure 3. Molecular packing diagram viewed down the *a* axis and highlighting the orientation of molecules in the two polymorphic forms, with hydrogen atoms omitted for clarity. The diagrams are generated using Mercury.⁴²

fractions of H···H and O···H contacts and these two types of contacts together contribute 77% of the total contacts. The major differences in intermolecular contacts are seen for C···H (i.e., C–H··· π) and "other" types of contacts. The yellow form contains a higher fraction (21%) of C···H contacts compared to that of the orange form (16%). The yellow form contains only 2% (with neither O···O nor N···H contacts) of "other" contacts and the orange form contains 7% of it. Further, quantitative and qualitative analyses of each of the intermolecular contacts are performed using the charge density distributions of these two polymorphs and discussed in the following sections. Here, our main focus is on the evaluation of charge density features associated with these two polymorphs.

Multipole Model and Deformation Densities. During the final refinement, the Hirshfeld rigid bond test⁴⁸ was applied to the covalent bonds involving non-hydrogen atoms. The values of maximum differences of mean-square displacement amplitudes are found to be $8(2) \times 10^{-4} \text{ \AA}^2$ at C(14)–N(15) in the orange form and $9(2) \times 10^{-4} \text{ \AA}^2$ at C(8)–C(9) in the yellow form, respectively, which are below the standard limit of 10^{-3} \AA^2 . The residual electron densities calculated (with $I > 3\sigma(I)$) over the molecular planes are almost featureless, the minimum and maximum densities are in the range of -0.223 to 0.130 e \AA^{-3} for the orange form and -0.195 to 0.249 e \AA^{-3} for the yellow form. The residuals are very similar to the values reported earlier on such polymorphic systems.^{14b} The static deformation electron density maps obtained from experimental and theoretical analyses of both crystal forms shown in Figure 5 are in good agreement and display expected bonding features. The electron lone pairs of all the O atoms, except the atoms affected by disorder, are clearly visible in the deformation electron density maps (also see Figure S1, Supporting Information). The deformation

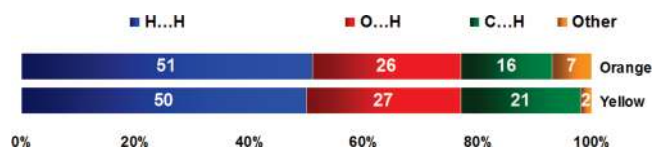


Figure 4. Relative contributions to the Hirshfeld surface areas for the various intermolecular contacts in the two polymorphs of coumarin 314.

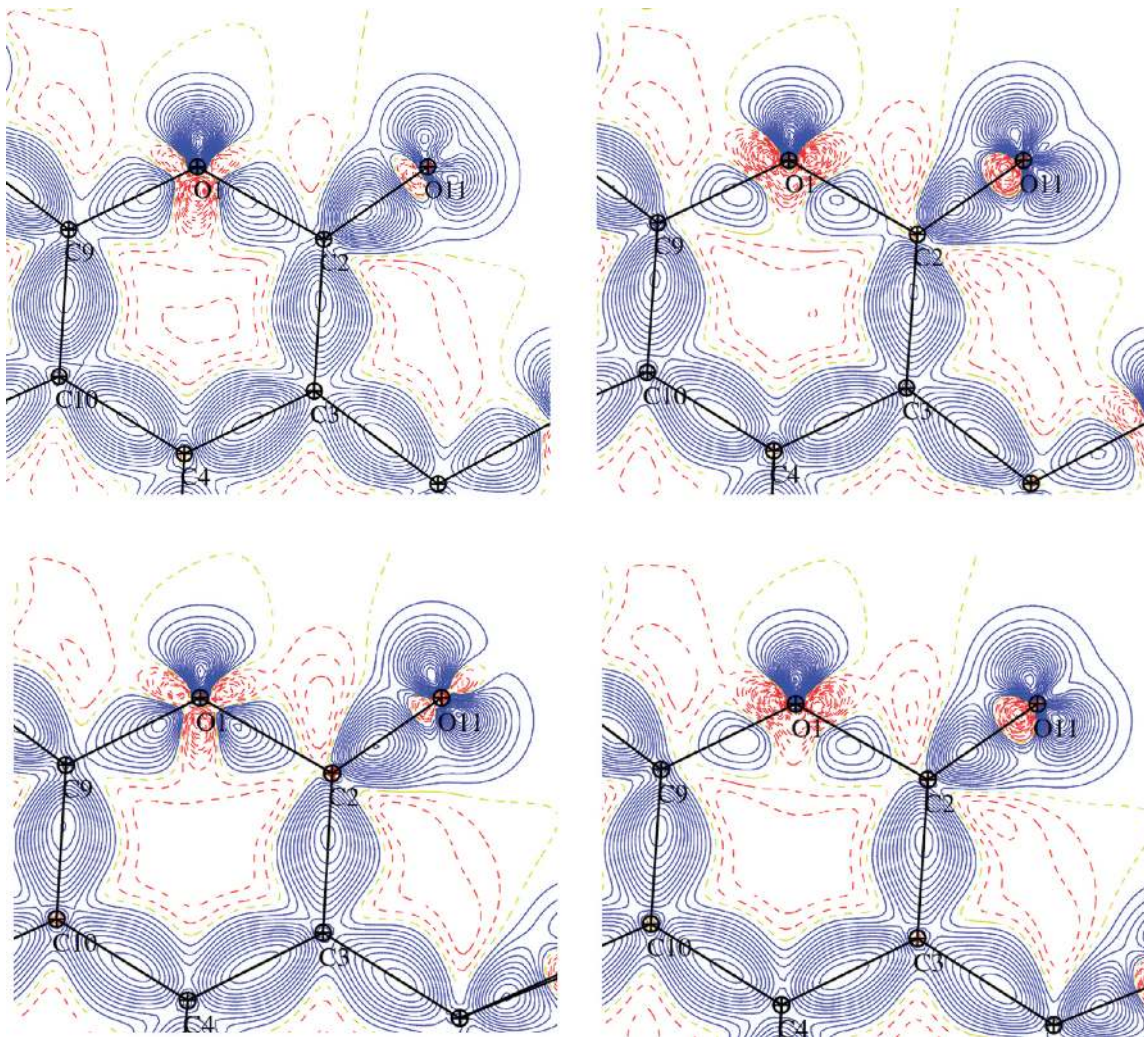


Figure 5. Static deformation density maps drawn in the plane containing atoms O1, O11, and C2, origin at atom O1. Contour intervals are at $\pm 0.05 \text{ e \AA}^{-3}$, positive and negative contours are in solid blue and broken red lines, respectively, and contour at zero level is shown as a broken yellow line.

electron density maps associated with the other parts of the molecules were also shown to have accurate bonding features.

A statistical analysis was performed on the static deformation electron density grids obtained from the experimental and theoretical multipole modeling of the two polymorphs. The correlation between the experimental and theoretical deformation electron densities $\Delta\rho$ is 95% and 92% for the orange and the yellow forms, respectively. The diffraction data of the orange crystal form are of slightly better quality in terms of resolution and R -factors, which is in accordance with the higher correlation.

Topology of Covalent Bonds. The topological analysis of the total electron density $\rho(r)$ and the localization of the BCP were performed using VMoPro, a properties visualization tool of the MoPro software.²⁹ The topological parameters of the covalent bonds are listed in Table S1 in the Supporting Information. The experimental and theoretical values of the two forms are in good agreement, demonstrating that both methodologies provide a consistent measure of the topological properties of the charge densities. The topological parameters (covalent bond length (d), electron density (ρ_b), and Laplacian ($\nabla^2\rho_b$)) of covalent bonds involving non-hydrogen atoms of the two crystal forms, obtained from experiment and theory, are compared and shown in Figure S2,

Supporting Information. The d values of these two polymorphic forms are found to follow a linear trend. The experimental and the theoretical values of d are also found to follow a similar trend. The values of ρ_b and $\nabla^2\rho_b$ obtained from the experimental and theoretical analyses seem to follow a slight different trend; theoretical values tend to be a little higher than the experimental values. However, these values are found to be comparable between the two polymorphic forms. As expected, in terms of the values of topological properties, in both forms the C=O bonds are found to be the strongest one (Table S1, Supporting Information). Conversely, in both forms the bond O21–C22 has the lowest values of ρ_b and the highest values of $\nabla^2\rho_b$ and thus the weakest bond. From both methods and in both forms, the values of ρ_b and $\nabla^2\rho_b$ of C–H bonds are found to agree well. The bond ellipticity (ϵ) values for all of the covalent bonds in both forms are within their expectation limits.

Topology of Intermolecular Interactions. Table 2 summarizes the experimental and theoretical values of topological parameters (R_{ij} , ρ_b , and $\nabla^2\rho_b$), the energy densities ($G(r_{CP})$ and $V(r_{CP})$), and the total electrostatic interaction energies ($E_{es,tot}$) of the intermolecular interactions present in both forms. A number of C–H \cdots O, C–H \cdots π , and $\pi\cdots\pi$ type of intermolecular contacts have been identified in these two polymorphic forms of coumarin 314 dye (Table 2).

Table 2. Topological Features of Intermolecular Contacts with O or π Acceptors and $\pi \cdots \pi$ Interactions^a

Orange									
bond (A–B)	<i>d</i> (Å)	<i>r</i> ₁ (Å)	<i>r</i> ₂ (Å)	ρ_b (e Å ⁻³)	$\nabla^2\rho_b$ (e Å ⁻⁵)	<i>G</i> (<i>r</i> _{CP}) (kJ mol ⁻¹ bohr ⁻³)	<i>V</i> (<i>r</i> _{CP}) (kJ mol ⁻¹ bohr ⁻³)	<i>E</i> _{es,tot} (kJ mol ⁻¹)	
O11⋯H5 ⁱ	2.3906	1.4046	0.9933	0.08	0.69	16.83	-14.98	-22	
	2.3078	1.3820	0.9280	0.08	0.91	21.36	-17.83	-31	
O11⋯H13A ⁱⁱ	2.3769	1.4231	0.9561	0.07	0.77	17.67	-14.43	-78 ^b	
	2.3431	1.3918	0.9521	0.08	0.88	21.02	-18.15	-96 ^b	
O20⋯H16B	2.6526	1.5629	1.0936	0.06	0.50	12.06	-10.55		
	2.6102	1.5358	1.0792	0.06	0.57	13.58	11.68		
O21⋯N15	3.5661	1.7675	1.8450	0.02	0.32	6.20	-3.79		
	3.6484	1.7689	1.8909	0.02	0.31	6.05	-3.62		
O11⋯H16A ⁱⁱⁱ	2.4661	1.4489	1.0221	0.07	0.72	17.01	-14.38	-36	
	2.4500	1.4500	1.0021	0.07	0.78	17.91	-14.54	-25	
O11⋯H23C ^{iv}	2.7479	1.5506	1.2908	0.03	0.58	11.52	-7.36	-14	
	2.6112	1.5017	1.1115	0.04	0.72	14.79	-9.95	-3	
O20⋯H12B ^v	2.5740	1.4915	1.0838	0.04	0.70	14.36	-9.57	-21	
	2.5765	1.4922	1.0850	0.04	0.72	14.72	-9.82	-13	
O20⋯H17A ^{vi}	2.6555	1.5381	1.1266	0.04	0.42	9.02	-6.49	3	
	2.6193	1.5005	1.1266	0.05	0.50	10.94	-8.36	-4	
C3⋯H22B ^{vii}	2.8860	1.7957	1.1277	0.05	0.37	8.80	-7.49	6 ^b	
	2.8299	1.7458	1.1215	0.06	0.43	10.88	-9.93	-2 ^b	
C4⋯H22B	2.7478	1.7008	1.1277	0.05	0.37	8.80	-7.49		
	2.6832	1.6549	1.1215	0.06	0.43	10.88	-9.93		
O20⋯O20	3.3461	1.6731	1.6730	0.03	0.49	9.92	-6.60		
	3.4190	1.7098	1.7092	0.03	0.46	9.35	-6.12		
C19⋯C19	3.6091	1.8045	1.8047	0.03	0.49	9.92	-6.60		
	3.5393	1.7692	1.7701	0.03	0.46	9.35	-6.12		
C5⋯H14B ^{viii}	2.8003	1.6378	1.1683	0.05	0.35	8.69	-7.74	-63 ^b	
	2.8389	1.6520	1.1931	0.05	0.35	8.32	-7.09	-25 ^b	
C6⋯H14B	2.9660	1.9737	1.1683	0.05	0.35	8.69	-7.74		
	3.0218	2.0104	1.1931	0.05	0.35	8.32	-7.09		
C7⋯H12A	2.6506	1.5691	1.1019	0.06	0.52	12.16	-10.27		
	2.6494	1.5676	1.1001	0.06	0.54	12.60	-10.47		
C8⋯H12A	3.0863	2.2038	1.1019	0.06	0.52	12.16	-10.27		
	3.0804	2.1998	1.1001	0.06	0.54	12.60	-10.47		
N15⋯H12A	2.7591	1.7767	1.1019	0.06	0.52	12.16	-10.27		
	2.7568	1.7806	1.1001	0.06	0.54	12.60	-10.47		
C6⋯H23C ^{ix}	3.1258	1.8958	1.2306	0.03	0.26	5.39	-3.77	5	
	3.2125	1.8658	1.3528	0.02	0.26	5.30	-3.54	3	
Yellow									
bond (A–B)	<i>d</i> (Å)	<i>r</i> ₁ (Å)	<i>r</i> ₂ (Å)	ρ_b (e Å ⁻³)	$\nabla^2\rho_b$ (e Å ⁻⁵)	<i>G</i> (<i>r</i> _{CP}) (kJ mol ⁻¹ bohr ⁻³)	<i>V</i> (<i>r</i> _{CP}) (kJ mol ⁻¹ bohr ⁻³)	<i>E</i> _{es,tot} (kJ mol ⁻¹)	
O11⋯H4 ⁽ⁱ⁾	2.5275	1.4435	1.0878	0.06	0.63	14.25	-11.22	-33	
	2.5215	1.4723	1.0524	0.05	0.59	12.89	-9.63	-41	
O11⋯H5	2.7042	1.5371	1.1833	0.04	0.46	9.82	-7.03		
	2.6703	1.5464	1.1368	0.04	0.46	9.60	-6.76		
O20A⋯H5	2.4465	1.4442	1.0136	0.07	0.85	19.34	-15.41		
	2.3848	1.4133	0.9741	0.07	0.85	19.00	-14.71		
O20A⋯H12B	2.3489	1.3909	0.9605	0.08	1.01	22.64	-17.76		
	2.2839	1.3551	0.9315	0.09	0.98	23.78	-20.75		
O11⋯H13A ⁽ⁱⁱ⁾	2.6990	1.5418	1.1657	0.04	0.57	11.45	-7.49	-75 ^b	
	2.6403	1.5204	1.1202	0.04	0.62	12.74	-8.61	-76 ^b	
O11⋯H14A	2.7029	1.5450	1.1667	0.04	0.62	12.58	-8.35		
	2.6015	1.5103	1.0934	0.05	0.72	14.97	-10.21		
C10⋯H18A	2.6738	1.6160	1.0645	0.06	0.56	12.89	-10.48		
	2.7248	1.6028	1.1230	0.06	0.46	11.00	-9.50		
O11⋯H17A ⁽ⁱⁱⁱ⁾	2.7705	1.5313	1.3609	0.04	0.59	11.94	-7.93	-30 ^b	
	2.6962	1.5124	1.2818	0.04	0.69	14.04	-9.38	-33 ^b	
O11⋯H17B	2.8905	1.5313	1.5521	0.04	0.59	11.94	-7.93		
	2.8089	1.5126	1.5328	0.04	0.69	14.04	-9.37		
O20A⋯H22B ^(iv)	2.4912	1.4440	1.0498	0.05	0.72	14.99	-10.31	9 ^b	
	2.4989	1.4532	1.0549	0.06	0.70	15.84	-12.54	-21 ^b	
O21⋯H13A ^(v)	2.7175	1.5502	1.1787	0.04	0.61	12.28	-8.03	-7	
	2.7156	1.5515	1.1663	0.03	0.59	11.77	-7.61	-9	
C4⋯H13B	3.1379	2.0606	1.3882	0.02	0.19	3.90	-2.52		
	3.1881	1.9662	1.3877	0.02	0.20	4.06	-2.58		
O21⋯H17A ^(vi)	2.5000	1.4620	1.0399	0.06	0.71	15.43	-11.58	-35 ^b	
	2.5855	1.4878	1.1016	0.05	0.60	13.01	-9.76	-31 ^b	
C2⋯H14B	3.0020	1.8194	1.2475	0.03	0.31	6.63	-4.82		
	3.0216	1.8277	1.2521	0.03	0.31	6.67	-4.94		
C3⋯H14B	3.0218	1.8343	1.2475	0.03	0.31	6.63	-4.82		
	3.0230	1.8383	1.2521	0.03	0.31	6.67	-4.94		

Table 2. Continued

Yellow									
bond (A–B)	<i>d</i> (Å)	<i>r</i> ₁ (Å)	<i>r</i> ₂ (Å)	ρ_b (e Å ⁻³)	$\nabla^2\rho_b$ (e Å ⁻⁵)	<i>G</i> (<i>r</i> _{CP}) (kJ mol ⁻¹ bohr ⁻³)	<i>V</i> (<i>r</i> _{CP}) (kJ mol ⁻¹ bohr ⁻³)	<i>E</i> _{cs,tot} (kJ mol ⁻¹)	
C10···H16A	3.1608	2.0774	1.1892	0.04	0.41	8.83	-6.38		
	<i>3.1061</i>	<i>2.0017</i>	<i>1.1781</i>	<i>0.04</i>	<i>0.40</i>	<i>8.60</i>	<i>-6.33</i>		
C3···H16B ^(vii)	2.6960	1.5880	1.1084	0.06	0.50	11.74	-9.92	3	
	<i>2.7140</i>	<i>1.5937</i>	<i>1.1242</i>	<i>0.06</i>	<i>0.47</i>	<i>11.40</i>	<i>-10.00</i>	<i>13</i>	
C5···H22A ^(viii)	2.9606	2.0270	1.1569	0.04	0.44	9.27	-6.46	-35	
	<i>2.9940</i>	<i>1.8755</i>	<i>1.1808</i>	<i>0.05</i>	<i>0.37</i>	<i>8.72</i>	<i>-7.25</i>	<i>-32</i>	
C6···H22A	2.8959	1.7535	1.1569	0.04	0.44	9.27	-6.46		
	<i>2.8735</i>	<i>1.7405</i>	<i>1.1808</i>	<i>0.05</i>	<i>0.37</i>	<i>8.72</i>	<i>-7.25</i>		
C6···H23C ^(ix)	2.9396	1.8221	1.1356	0.03	0.32	6.55	-4.32	-7	
	<i>2.9238</i>	<i>1.7241</i>	<i>1.2094</i>	<i>0.04</i>	<i>0.33</i>	<i>7.57</i>	<i>-6.17</i>	<i>-8</i>	

^a *r*₁ and *r*₂ are the distances from the critical point to the first atom (A) and second atom (B), respectively. The interaction length, *R*_{ij} = (*r*₁ + *r*₂). Values in italics are from theoretical calculations. The symmetry codes are given in the second row under each interaction. The symmetry codes for the orange form are (i) *X* + 1/2; -*Y* + 3/2; *Z* + 1/2, (ii) -*X* + 1; -*Y* + 1; -*Z* + 1, (iii) -*X* + 3/2; *Y* + 1/2; -*Z* + 1/2, (iv) -*X* + 3/2; *Y* - 1/2; -*Z* + 3/2, (v) -*X* + 1/2; *Y* + 1/2; -*Z* + 1/2, (vi) *X* - 1/2; -*Y* + 3/2; *Z* + 1/2, (vii) -*X* + 1; -*Y* + 2; -*Z* + 1, (viii) -*X* + 1; -*Y* + 1; -*Z*, (ix) -*X* + 1/2; *Y* + 1/2; -*Z* - 1/2. The symmetry codes for the yellow form are (i) *X* + 1/2; -*Y* + 3/2; *Z* + 1/2, (ii) -*X* + 1; -*Y* + 1; -*Z* + 1 (iii) -*X* + 2; -*Y* + 1; -*Z* + 1, (iv) -*X* + 1; -*Y* + 2; -*Z* + 1, (v) -*X* + 1/2; *Y* + 1/2; -*Z* + 1/2, (vi) -*X* + 3/2; *Y* + 1/2; -*Z* + 1/2, (vii) -*X* + 3/2; *Y* + 3/2; -*Z* + 3/2, (viii) -*X* + 3/2; *Y* - 1/2; -*Z* + 1/2, (ix) -*X* + 1/2; *Y* - 1/2; -*Z* + 1/2. ^b Dimers with involutive symmetry operators.

As far as C–H···O intermolecular contacts are concerned, the two polymorphs are shown to have different networks of interactions. In both forms, no intermolecular BCPs were found involving atom O1. However, the atom O1 in the orange form seems to remotely interact with atom H16A, which forms a relatively strong hydrogen bond with the atom O11, the neighbor of atom O1 (Figure 6). No such interactions were observed for atom O1 of the yellow form. In the orange form, the atom O11 is involved in three relatively strong and one weak C–H···O contacts with *R*_{ij} in the range of 2.31–2.75 Å, ρ_b ; 0.03–0.08 e Å⁻³, $\nabla^2\rho_b$; 0.6–0.9 e Å⁻⁵, *G*(*r*_{CP}); 12–21 kJ mol⁻¹ bohr⁻³ and $|V(r_{CP})|$; 7–18 kJ mol⁻¹ bohr⁻³. The corresponding oxygen atom in the yellow form is involved in six such contacts but there are only five CPs. This is because of the common CP shared by two interactions between atom O11 and the atoms H17A and H17B. These interactions are relatively weak with *R*_{ij} in the range of 2.52–2.89 Å, ρ_b ; 0.04–0.06 e Å⁻³, $\nabla^2\rho_b$; 0.5–0.7 e Å⁻⁵, *G*(*r*_{CP}); 10–15 kJ mol⁻¹ bohr⁻³ and $|V(r_{CP})|$; 7–11 kJ mol⁻¹ bohr⁻³. The atom O20 in the orange form has three C–H···O contacts with *G*(*r*_{CP}) and $|V(r_{CP})|$ values ranging from 9–15 kJ mol⁻¹ bohr⁻³ and 6–12 kJ mol⁻¹ bohr⁻³, respectively. In the yellow form, the corresponding atom O20A also has three such intermolecular contacts but with higher values of *G*(*r*_{CP}) (15–24 kJ mol⁻¹ bohr⁻³) and $|V(r_{CP})|$ (10–21 kJ mol⁻¹ bohr⁻³). Although there is no C–H···O contact involving atom O21 in the orange form, there are two such intermolecular contacts present in the yellow form (Table 2).

As expected for colored dyes, there are number of C–H···π interactions present in the two crystal forms. These π electrons are either from carbon atoms or from the aromatic bonds involving those carbon atoms. As seen from Table 2, these interactions are mainly concentrated in the vicinity of the rings of the coumarin moiety in both crystal forms. There is only one such interaction involving the atom N15, which is present in the orange form. The atom H22B in the orange form is interacting with the atoms C3 and C4 via a common CP, indicating that this hydrogen atom is essentially interacting with the π electrons of the C3–C4 bond. A similar scenario is observed for atom H14B, with the π electrons of the C5–C6 bond. The atom H12A is found to be interacting with the π electrons of three bonded atoms

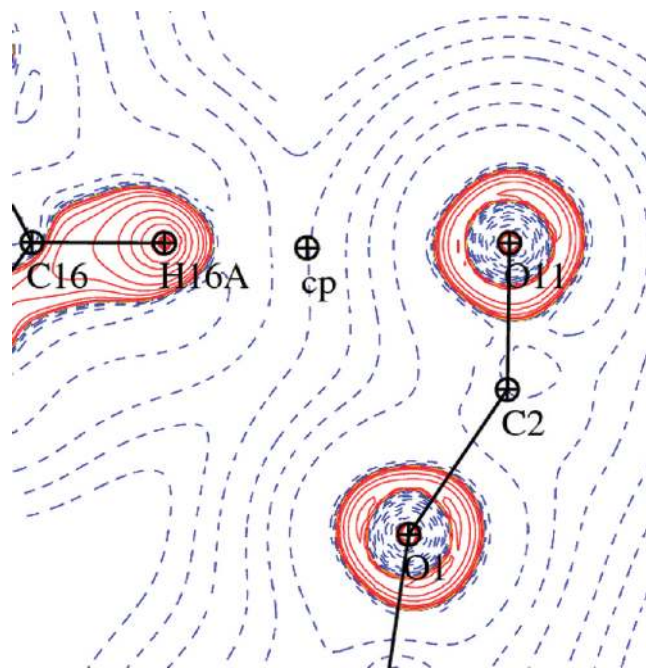


Figure 6. Laplacian [$\nabla^2\rho_b(\mathbf{r})$] distribution of one of the C–H···O intermolecular interactions in the orange form. The map is drawn in the plane containing atoms O1, O11, and H16A and with the origin at atom H16A. Solid blue and broken red lines represent positive and negative contours, respectively. Contours are drawn at $\pm 2 \times 10^9$, $\pm 4 \times 10^9$, $\pm 8 \times 10^9$ ($n = -3$ to $+3$) e Å⁻⁵ levels.

N15–C7–C8 via a common CP as well. There are two such cases observed in the yellow form: one of them is between atom H14B and the bond C2–C3 and the other one is between atom H22A and the bond C5–C6. Overall, the strengths of these interactions are found to be similar in both forms and compares well with their corresponding theoretical values. The values of *G*(*r*_{CP}) and $|V(r_{CP})|$ range from 5–13 kJ mol⁻¹ bohr⁻³ and 4–10 kJ mol⁻¹ bohr⁻³, respectively, for the orange form, and the corresponding values for the yellow form are 4–13 kJ mol⁻¹ bohr⁻³ and 3–10 kJ mol⁻¹ bohr⁻³ respectively.

The other type of intermolecular interactions involving π electrons, the π···π interactions, is of extreme importance

in the context of colored dyes. The orange form is found to have three such contacts (Table 2), two of them between the same type of atoms ($O20 \cdots O20$ and $C19 \cdots C19$) and the other one is between two different types of atoms ($O21 \cdots N15$). However, no such contacts were found in the yellow form. This is mainly due to the shorter interplanar distance between the molecules in the orange form (3.5562(4) Å) compared to those in the yellow form (3.6581(3) Å), as mentioned before. Consequently, a variation of color is seen in these two polymorphic dye crystals.

For both crystal forms, the total electrostatic interaction energies ($E_{es,tot}$) between the dimers involved in $C-H \cdots O$, $C-H \cdots \pi$, and $\pi \cdots \pi$ types of contacts were computed based on their experimental and theoretical electron densities (Table 2). The methodology for the calculation of $E_{es,tot}$ using VMOPro is discussed elsewhere.⁴⁹ The electrostatic interaction energies were summed for all these dimers, with a weighting of one-half for dimers with involutive symmetry operators. For the orange form, the summation of $E_{es,tot}$ is -152 kJ mol^{-1} (experimental) and -134 kJ mol^{-1} (theoretical), and for the yellow form the corresponding values are -162 kJ mol^{-1} (experimental) and -173 kJ mol^{-1} (theoretical). From these results, it appears that the orange form has weaker electrostatic interaction energies compared to the yellow form. However, the values of $E_{es,tot}$ between the polymorphs are closely related.

The experimental and theoretical values of topological parameters including energy densities and the total electrostatic interaction energies of the dimers of the orange and the yellow forms are in agreement (Table 2). However, the subtle differences between the experimental and theoretical topological values and especially for intermolecular bond lengths are because the theoretical results are based on the optimized geometry obtained from periodic quantum calculations, whereas the experimental results are from experimental crystal geometries. It is, in this context, to be noted that the energy difference between the crystals with optimized geometry and with experimental geometry is -42 and -63 kJ mol^{-1} for the orange form and the yellow form, respectively. The topological properties, such as electron densities, Laplacian and local kinetic and potential energy densities of both of these polymorphic forms are also comparable to earlier such studies^{36,50} and seem to correlate well with the interaction lengths.⁵¹

Electrostatic Potentials. Analysis of deformation electrostatic potential (ESP) derived from the deformation electron densities on the molecular surfaces was performed to highlight the effect of crystalline environment and also to point out the differences and the similarities between the two polymorphic forms. The construction of a three-dimensional ESP map plotted over the molecular surfaces from experimental charge densities clearly brings out the differences of electrostatic nature of the two forms (Figure 7). The electropositive and electronegative surfaces are well separated in both forms. The orange form displays a larger electronegative surface compared to the yellow form. This is due to the conformational difference at the ethoxycarbonyl side chain and additionally due to the involvement of the π electrons of three bonded atoms $N15-C7-C8$ in $C-H \cdots \pi$ type of contacts and the presence of $\pi \cdots \pi$ contacts in the orange form (Table 2). As expected, in both polymorphs, the spread of electronegative surface is mainly seen around the oxygen atoms, which are involved in $C-H \cdots O$ type of intermolecular contacts. However, the atom O1 in the yellow form is shown to have less prominent electronegative surface compared to other O atoms in the structures. This is because the atom O1 is not involved in any intermolecular contacts, whereas the corresponding atom in the orange form is seen to interact remotely with the neighbor molecule (see Figure 6). These ESP maps correlate well with the observations of intermolecular contacts (Table 2) as discussed in the previous section. The corresponding maps from the theoretical analysis revealed similar features. The ESP maps clearly emphasize the preferred binding sites to form the networks of interactions and also highlight the difference in nature of interactions in the two polymorphic forms.

Lattice Energies. The lattice energies, defined as the difference between the molecular interaction energy in crystal and the molecular relaxation energy upon sublimation, were calculated according to the procedure outlined by Abramov et al.⁵³ The package CRYSTAL06 was used to calculate the molecular interaction energies, which is essentially the difference between the energy of the molecule in the crystal and that of the isolated molecule with crystal geometry. The basis set superposition error was corrected by adopting the counterpoise method.⁵⁴ Relaxation energies, which measure the difference between the energy of the isolated molecule with optimized geometry and the molecule with crystal geometry,

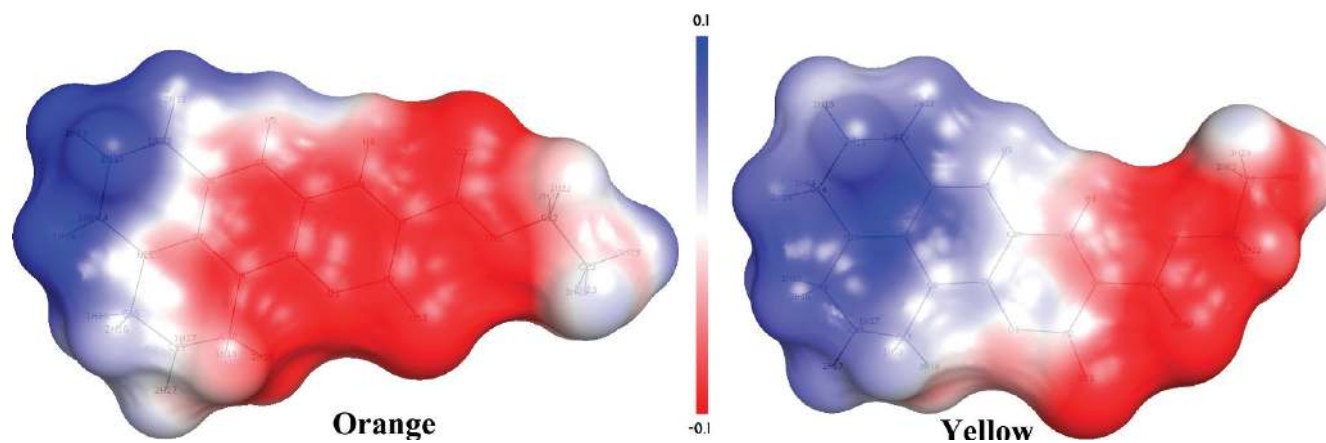


Figure 7. Experimental deformation electrostatic potential $\Delta\phi$ ($e \text{ \AA}^{-1}$) plotted over the molecular surfaces of coumarin 314, orange form (left) and yellow form (right). The potential of $+0.1 e \text{ \AA}^{-1}$ is shown in blue and $-0.1 e \text{ \AA}^{-1}$ in red. The potential $\Delta\phi$ is derived from the deformation electron density $\Delta\rho$. The diagrams are generated with Pymol.⁵²

were calculated using GAUSSIAN03⁵⁵ with DFT method at the B3LYP/6-31G(d,p) level of theory.

The orange form is shown to have weaker interaction energy ($-26.3 \text{ kJ mol}^{-1}$) compared to the yellow form ($-42.0 \text{ kJ mol}^{-1}$). It is to be noted that, whether it is from experimental geometry or from theoretically optimized geometry, the same as above interaction energy values were obtained for both forms. The relaxation energy of the orange form (7.9 kJ mol^{-1}) is as low as half of the yellow form (15.8 kJ mol^{-1}). Therefore, the orange form has weaker lattice energy of $-18.4 \text{ kJ mol}^{-1}$ compared to the yellow form with lattice energy of $-26.3 \text{ kJ mol}^{-1}$. However, these two lattice energies are closely related and this clarifies the cause of occurrence of polymorphism in coumarin 314. These observations are in accordance with the results of $E_{\text{es,tot}}$ obtained from the charge density distributions as discussed above (Table 2). However, from these results, it is tempting to conclude that the yellow form is thermodynamically the favored form compared to the orange form.

The single point energies of isolated free molecules calculated using GAUSSIAN03 revealed that the polymorphs with two distinct conformations have almost equal energies. The energy difference between the two forms is only 16.0 kJ mol^{-1} . This observation once again supports the cause of the occurrences of two polymorphic structures of coumarin 314 dye.

Atomic Charges. The values of atomic charges derived from the experimental and theoretical multipole refinements of the two polymorphs are listed in Table S2, Supporting Information. From each method, it is noticed that the atoms in these two polymorphic forms carry rather different charges. In each case, the electronegative oxygen and nitrogen atoms are found to carry negative charges. However, the ester oxygen atoms have higher charges than the carbonyl oxygen atoms. In the orange form, the atoms C2 and C19, bonded to two electronegative oxygen atoms, are either a little negatively charged (experiment) or a little positively charged (theory). The corresponding atoms in the yellow form are almost neutral within the estimated standard deviations or negatively charged (atom C19, experiment). It is to be noted that in the yellow form, the atom C19 is bonded to atoms O20 and O21 whose multipole populations are transferred from the theoretical model. In each case, the atom C9 bonded to the ester oxygen atom of the coumarin moiety carrying slightly negative charges, whereas the atom C22 of $>\text{CH}_2$ group, with negative charges on hydrogen atoms, bonded to the other ester oxygen atom carrying positive charges. The hydrogen atoms are negatively charged and are in agreement with the UBDB theoretical electron density database.⁵⁶ It is to be noted that the atomic charges ($N_{\text{val}} - P_{\text{val}}$), derived from the Hansen & Coppens multipole formalism,³⁰ do not take into account the charge transfer between atoms inherent to the dipoles. In the yellow form, the atoms H4 and H5 from the theoretical model are however found to carry a little positive charge; the corresponding carbon atoms have slightly negative charges. Similar charges were noticed for these types of atoms from other experimental and theoretical studies of this kind.^{14b,36,56} These appropriate atomic charges obtained from the multipole refinements certainly ensure the accuracy of the charge density models.

Dipole Moments. A quantitative charge density analysis of accurate single crystal X-ray diffraction data is capable of providing detailed information on the dipole moment of a

Table 3. Molecular Dipole Moments and Their Percentage Enhancements, Values Are in Debye^a

forms	μ_0	$\mu_{\text{X-ray}}$	$\% \Delta_{\text{X-ray}}$	μ_{theo}	$\% \Delta_{\text{theo}}$	μ_{LT}	$\% \Delta_{\text{LT}}$
orange	8.2	13.2	61	13.0	58	10.0	22
yellow	10.1	15.6	54	13.0	29	13.1	30

^aPercentage enhancement, $\% \Delta_{\text{X}} = 100 (\mu_0 - \mu_{\text{X}}) / \mu_0$; where X is either experimental (X-ray), theoretical (theo), or Lorentz factor Tensor (LT).

molecule in a crystal environment. However, the molecular dipole moments derived from such studies may often lead to pronounced enhancement compared to independent theoretical estimates.⁵⁷ This simplest one-electron property can have considerable significance in the context of polymorphism. The values of dipole moments, calculated from different approaches, are listed in Table 3. Almost from all approaches, the dipole moment value of the orange form is seen to be lower than the yellow form. The difference between the values of dipole moments obtained from experimental charge densities ($\mu_{\text{X-ray}}$) of the two forms is 2.4 D. However, no difference in dipole moment is observed from the calculation based on the multipole model refined with the theoretical structure factors (μ_{theo}). The difference is found to be 1.9 D, when the dipole moments were calculated on isolated single-molecules (μ_0) and based on optimized geometries obtained from periodic theoretical calculations. However, in both forms, the μ_0 values based on experimental geometries were very similar to the one listed here from optimized geometries. The dipole moments were also calculated using dipole lattice sums to estimate the electric field from Lorentz factor tensors (μ_{LT}).⁵⁸ These values are slightly lower compared to the values obtained from the experimental multipole models, and in this case the difference is 3.1 D. These last two calculations were performed with GAUSSIAN03 using the DFT method at B3LYP/6-31G(d,p) level of theory. Upon calculation of percentage enhancement with respect to μ_0 , the values of $\mu_{\text{X-ray}}$ of the orange and the yellow form showed a reasonable enhancement of 61 and 54%, respectively. Enhancement of this kind is well below the maximum acceptable enhancement of about 75% as stated in the detailed study on enhancement of dipole moments for a large number of molecules by Spackman et al.⁵⁷ For the orange form, the enhancement of μ_{theo} indicates a similar trend as seen in the case of $\mu_{\text{X-ray}}$ and a relatively smaller enhancement is noticed from the Lorentz tensor approach (Table 3). However, for yellow forms, similar enhancements of μ_{theo} and μ_{LT} are noticed, and the enhancements are smaller compared to the enhancement of $\mu_{\text{X-ray}}$. The magnitude of the polarizing field produced by the zero-field molecular dipoles of the orange form is found to be less than half (1.0 GV m^{-1}) of the yellow form (2.4 GV m^{-1}). However, in both cases, this field is closely parallel to the zero-field dipole, 15° and 25° for the orange and the yellow forms respectively. It is to be noted that comparatively a little larger difference of dipole moment values (3.1 D) between the polymorphs was seen from the Lorentz tensors approach, and it is due to the presence of higher magnitude of the polarizing field in the yellow form compared to the orange form.

Conclusions

The quantitative analyses of experimental and theoretical charge density distributions in two known conformational polymorphs of coumarin 314 dye have led to a better understanding of the variation of the charge density features

associated with the polymorphic structures in general. The presence of disorder at the carbonyl oxygen atom of ethoxy-carbonyl group in the yellow form, which was not identified earlier, is addressed here. On the other hand, the earlier study on the orange form at room temperature found some disorder at the carbon atom site of one of the piperidine ring systems but our present study at 100 K does not show any such disorder. The presence of disorder for a particular atom in the yellow form led us to transfer the multipoles and radial parameters of the agitated atoms from the corresponding theoretical model. The strategies of transferability of multipole parameters either from theoretical calculations or from the charge density database⁵⁹ is very encouraging to circumvent the challenging problem in performing multipole modeling of disordered structures from experimental charge density studies.

The values of topological properties of covalent bonds in these two crystal forms appeared to be comparable. Unlike the previous study,¹⁸ a variation in intermolecular interaction pattern is seen in these two conformational polymorphs. The quantification of intermolecular contacts via Hirshfeld surface analysis successfully revealed the differences and similarities between the polymorphs. The distinct networks of interactions with varying strengths are seen in these two polymorphs. The variation of colors of these polymorphic dyes is mainly due to the $\pi \cdots \pi$ interactions, which are present in the orange form only. The polymorphic forms are distinguishable in terms of their topological properties of intermolecular interactions. The summation of total electrostatic interaction energy values of the dimers suggests that the orange form has weaker electrostatic interaction energy compared to that of the yellow form. The plotting of three-dimensional deformation electrostatic potential maps over the molecular surfaces elucidates the difference in nature of interactions of these two polymorphs. Theoretical estimates of lattice energies indicate that the yellow form is thermodynamically the favored crystal form. The occurrence of polymorphism in coumarin 314 is believed to be due to the existence of two crystal forms with almost equal lattice energies and with two distinct conformations.

Slightly different atomic charges are noticed in these two polymorphs, with oxygen atoms generally more negative in the orange form. However, the dipole moment values obtained from multipole analysis and the theoretical approaches unravel these two polymorphs conveniently. The yellow form is shown to have indeed a slightly higher dipole moment. This is because of the conformational differences of the ethoxy-carbonyl group in the two forms, which brings two carbonyl groups together in the yellow form and approximately opposed in the orange form. This is also due to the higher magnitude of the polarizing field produced by zero-field molecular dipoles of the yellow form compared to the orange form. Lastly, this study is an additional contribution to the field of charge density analysis of polymorphic structures, which merit many more such studies.

Acknowledgment. P.M. thanks the European Commission for the award of Marie Curie International Incoming Fellowship within the seventh European Community Framework Programme. We thank Prof. Mark A. Spackman for providing his code for the calculation of electric field using Lorentz tensors and for his valuable comments on the results of dipole moments. We profusely thank the referees for their valuable comments and suggestions to improve our studies and the manuscript.

Supporting Information Available: Crystallographic information files (CIF) of both the polymorphs, static deformation density maps, topology of the covalent bonds involving the non-hydrogen atoms, figures of comparison of topologies in the two forms and the atomic charges. This information is available free of charge via the Internet at <http://pubs.acs.org/>.

References

- (1) (a) Hooper, D. C.; Wolfson, J. S.; McHugh, G. L.; Winters, M. B.; Swartz, M. N. *Antimicrob. Agents Chemother.* **1982**, *22*, 662–671. (b) Morris, A.; Russell, A. D. *Prog. Med. Chem.* **1971**, *8*, 39–59.
- (2) (a) Nemkovich, N. A.; Reis, H.; Baumann, W. *J. Lumin.* **1997**, *71*, 255–263 and the references therein. (b) Khalfan, H.; Abuknesha, R.; Rond-Weaver, M.; Price, R. G.; Robinson, R. *Histochem. J.* **1986**, *18* (9), 497–499.
- (3) Vishnumurthy, K.; Guru Row, T. N.; Venkatesan, K. In *Molecular and Supramolecular Photochemistry*; Ramamurthy, V., Schanze, K. S., Eds.; Marcel Dekker Inc.: New York, 2001; Vol. 8, pp 427–460.
- (4) Domagala, J. M.; Hagen, S. E.; Lunney, E. T.; Bradly, D., Warner-Lambert Co., US Patent No. 5510375, *A23*, **1996**.
- (5) Eid, A. I.; Ragab, F. A.; El-Ansary, S. L.; El-Gazayerly, S. M.; Mourad, F. E. *Arch. Pharm.* **1994**, *327*, 211–213.
- (6) Reynolds, J. E. F. In *Martindale: The Extra Pharmacopoeia*, 30th ed.; The Pharmaceutical Press: London, 1993.
- (7) Jasinski, J. P.; Paight, E. S. *Acta Crystallogr.* **1994**, *C50*, 1928–1930.
- (8) Jasinski, J. P.; Woudenberg, R. C. *Acta Crystallogr.* **1995**, *C51*, 107–109.
- (9) (a) Gridunova, G. V.; Yufit, D. S.; Struchkov, Yu. T.; Khrolova, O. R.; Reznichenko, A. Z.; Tavrizova, M. A. *Kristallografiya* **1992**, *37*, 366–372. (b) Yip, B.-C.; Moo, F.-M.; Lok, K.-S.; Fun, H.-K.; Sivakumar, K. A. *Acta Crystallogr.* **1996**, *C52*, 477–481.
- (10) Yip, B.-C.; Fun, H.-K.; Sivakumar, K.; Zhou, Z.-Y.; Shawkataly, O. B.; Teoh, S.-G. *Acta Crystallogr.* **1995**, *C51*, 956–958.
- (11) Honda, T.; Fujii, I.; Hirayama, N.; Aoyama, N.; Miike, A. *Acta Crystallogr.* **1996**, *C52*, 395–397.
- (12) Bernstein, J. *Polymorphism in Molecular Crystals*; Oxford University Press: Oxford, Great Britain, 2002.
- (13) Moorthy, J. N.; Venkatesan, K. *Bull. Chem. Soc. Jpn.* **1994**, *67*, 1–6.
- (14) (a) Munshi, P.; Venugopala, K. N.; Jayashree, B. S.; Guru Row, T. N. *Cryst. Growth Des.* **2004**, *4* (6), 1105–1107. (b) Munshi, P.; Guru Row, T. N. *Cryst. Growth Des.* **2006**, *6* (3), 708–718.
- (15) Vishnumurthy, K.; Guru Row, T. N.; Venkatesan, K. *Photochem. Photobiol. Sci.* **2002**, *1*, 799–802.
- (16) (a) Bernstein, J. *Prog. Clin. Biol. Res.* **1989**, *289*, 203–215. (b) Brittain, H. G. *Polymorphism in Pharmaceutical Solids*; Marcel Dekker: New York, 1999; Vol. 95.
- (17) (a) Schmidt, G. M. J. *Pure Appl. Chem.* **1971**, *27*, 647–678. (b) Desiraju, G. R. *Crystal Engineering. The Design of Organic Solids*; Elsevier: Amsterdam, 1989.
- (18) Overgaard, J.; Hibbs, D. E. *Acta Crystallogr.* **2004**, *A60*, 480–487.
- (19) (a) Kulkarni, G. U.; Kumaradhas, P.; Rao, C. N. R. *Chem. Mater.* **1998**, *10*, 3498–3505. (b) Gopalan, R. S.; Kulkarni, G. U.; Rao, C. N. R. *ChemPhysChem* **2000**, *1*, 127–135. (c) Whitten, A. E.; Dittrich, B.; Spackman, M. A.; Turner, P.; Brown, T. C. *Dalton Trans.* **2004**, 23–29.
- (20) Hohenberg, P.; Kohn, W. *Phys. Rev. B* **1964**, *136*, 864–871.
- (21) (a) Bader, R. F. W. *Atoms in Molecules—A Quantum Theory*; Clarendon: Oxford, 1990. (b) Bader, R. F. W. *J. Phys. Chem.* **1998**, *A102*, 7314–7323.
- (22) Abramov, Yu. A. *Acta Crystallogr.* **1997**, *A53*, 264–272.
- (23) COLLECT; Nonius B V, Delft, The Netherlands, 1998.
- (24) Otwinowski, Z.; Minor, W. *Methods in Enzymology, Macromolecular Crystallography, Part A*; Carter, C. W., Jr.; Sweet, R. M., Eds.; Academic Press: New York, 1997; Vol. 279, pp 307–326.
- (25) Blessing, R. H. *J. Appl. Crystallogr.* **1997**, *30*, 421–426.
- (26) Altomare, A.; Cascarano, G.; Giacovazzo, C.; Guagliardi, A. *J. Appl. Crystallogr.* **1993**, *26*, 343–350.
- (27) Sheldrick, G. M. *Acta Crystallogr.* **2008**, *A64*, 112–122.
- (28) Farrugia, L. J. *WinGX (Version 1.80.03)*. *J. Appl. Crystallogr.* **1999**, *32*, 837–838.
- (29) (a) Guillot, B.; Viry, L.; Guillot, R.; Lecomte, C.; Jelsch, C. *J. Appl. Crystallogr.* **2000**, *34*, 214–223. (b) Jelsch, C.; Guillot, B.; Lagoutte, A.; Lecomte, C. *J. Appl. Crystallogr.* **2005**, *38*, 38–54.
- (30) Hansen, N. K.; Coppens, P. *Acta Crystallogr.* **1978**, *A34*, 909–921.
- (31) Stewart, R. F.; Davidson, E. R.; Simpson, W. T. *J. Chem. Phys.* **1965**, *42*, 3175–3187.
- (32) Clementi, E.; Raimondi, D. L. *J. Chem. Phys.* **1963**, *38*, 2686–2689.

- (33) Kissel, L.; Zhou, B.; Roy, S. C.; Sen Gupta, S. K.; Pratt, R. H. *Acta Crystallogr.* **1995**, *A51*, 271–288.
- (34) (a) Madsen, A. O. *J. Appl. Crystallogr.* **2006**, *39*, 757–758. (b) Munshi, P.; Madsen, A. O.; Spackman, M. A.; Larsen, S.; Destro, R. *Acta Crystallogr.* **2008**, *A64*, 465–475.
- (35) Dovesi, R.; Saunders, V. R.; Roetti, C.; Orlando, R.; Zicovich-Wilson, C. M.; Pascale, F.; Civalleri, B.; Doll, K.; Harrison, N. M.; Bush, I. J.; D'Arco, Ph.; Llunell, M. *CRYSTAL06 User's Manual*; University of Torino: Torino, 2006.
- (36) (a) Munshi, P.; Guru Row, T. N. *J. Phys. Chem. A* **2005**, *109*, 659–672. (b) Munshi, P.; Cameron, E.; Cameron, T. S.; Guru Row, T. N.; Ferrara, J. D. *J. Phys. Chem. A* **2007**, *111*, 7888–7897.
- (37) Allen, F. H.; Watson, D. G.; Brammer, L.; Orpen, A. G.; Taylor, R. *International Tables for Crystallography*; Springer: New York, 2006; Vol. C, Chapter 9.5, pp 790–811.
- (38) Volkov, A.; Gatti, C.; Abramov, Yu.; Coppens, P. *Acta Crystallogr.* **2002**, *A56*, 252–258.
- (39) (a) Dittrich, B.; Warren, J. E.; Fabbiani, F. P. A.; Morgenroth, W.; Corry, B. *Phys. Chem. Chem. Phys.* **2009**, *11*, 2601–2609. (b) Bak, J. M.; Dominiak, P. M.; Wilson, C. C.; Wozniak, K. *Acta Crystallogr.* **2009**, *A65*, 490–500.
- (40) (a) Johnson, C. K.; Burnett, M. N. *ORTEP-III*; Report ORNL-6895; Oak Ridge National Laboratory, Oak Ridge, TN, 1996. (b) Farrugia, L. J. *J. Appl. Crystallogr.* **1997**, *30*, 565.
- (41) *Persistence of Vision Raytracer (Version 3.6)*; Persistence of Vision Pty. Ltd: Williamstown, Victoria, Australia, **2004**; Retrieved from <http://www.povray.org/download/>.
- (42) Macrae, C. F.; Edgington, P. R.; McCabe, P.; Pidcock, E.; Shields, G. P.; Taylor, R.; Towler, M.; van de Streek, J. *J. Appl. Crystallogr.* **2006**, *39*, 453–457.
- (43) Nardelli, M. *Comput. Chem.* **1983**, *7*, 95–98.
- (44) (a) McKinnon, J. J.; Spackman, M. A.; Mitchell, A. S. *Acta Crystallogr.* **2004**, *B60*, 627–668. (b) Spackman, M. A.; McKinnon, J. J. *CrystEngComm* **2002**, *4*, 378–392.
- (45) Wolff, S. K.; Grimwood, D. J.; McKinnon, J. J.; Jayatilaka, D.; Spackman, M. A.; *CrystalExplorer 2.0*; University of Western Australia: Perth, 2007; <http://hirshfeldsurface.net/CrystalExplorer>.
- (46) McKinnon, J. J.; Jayatilaka, D.; Spackman, M. A. *Chem. Commun.* **2007**, 3814–3816.
- (47) Munshi, P.; Skelton, W.; McKinnon, J. J.; Spackman, M. A. *CrystEngComm* **2008**, *10*, 197–206.
- (48) Hirshfeld, F. L. *Acta Crystallogr.* **1976**, *A32*, 239–244.
- (49) Fournier, B.; Bendeif, El-E; Guillot, B.; Podjarny, A.; Lecomte, C.; Jelsch, C. *J. Am. Chem. Soc.* **2009**, *131*, 10929–10941.
- (50) Mallinson, P. R.; Smith, G. T.; Wilson, C. C.; Grech, E.; Wozniak, K. *J. Am. Chem. Soc.* **2003**, *125*, 4259–4270.
- (51) Munshi, P.; Guru Row, T. N. *CrystEngComm* **2005**, *7*, 608–611.
- (52) DeLano, W. L. *The PyMOL Molecular Graphics System*; DeLano Scientific: San Carlos, CA, 2002; <http://www.pymol.org>.
- (53) Abramov, Y. A.; Volkov, A.; Wu, G.; Coppens, P. *J. Phys. Chem. B* **2000**, *104*, 2183–2188.
- (54) Boys, S. F.; Bernardi, F. *Mol. Phys.* **1970**, *19*, 553–566.
- (55) Gaussian 03, Revision C.02, Frisch, M. J.; Trucks, G. W.; Schlegel, H. B.; Scuseria, G. E.; Robb, M. A.; Cheeseman, J. R.; Montgomery, J. A., Jr.; Vreven, T.; Kudin, K. N.; Burant, J. C.; Millam, J. M.; Iyengar, S. S.; Tomasi, J.; Barone, V.; Mennucci, B.; Cossi, M.; Scalmani, G.; Rega, N.; Petersson, G. A.; Nakatsuji, H.; Hada, M.; Ehara, M.; Toyota, K.; Fukuda, R.; Hasegawa, J.; Ishida, M.; Nakajima, T.; Honda, Y.; Kitao, O.; Nakai, H.; Klene, M.; Li, X.; Knox, J. E.; Hratchian, H. P.; Cross, J. B.; Bakken, V.; Adamo, C.; Jaramillo, J.; Gomperts, R.; Stratmann, R. E.; Yazyev, O.; Austin, A. J.; Cammi, R.; Pomelli, C.; Ochterski, J. W.; Ayala, P. Y.; Morokuma, K.; Voth, G. A.; Salvador, P.; Dannenberg, J. J.; Zakrzewski, V. G.; Dapprich, S.; Daniels, A. D.; Strain, M. C.; Farkas, O.; Malick, D. K.; Rabuck, A. D.; Raghavachari, K.; Foresman, J. B.; Ortiz, J. V.; Cui, Q.; Baboul, A. G.; Clifford, S.; Cioslowski, J.; Stefanov, B. B.; Liu, G.; Liashenko, A.; Piskorz, P.; Komaromi, I.; Martin, R. L.; Fox, D. J.; Keith, T.; Al-Laham, M. A.; Peng, C. Y.; Nanayakkara, A.; Challacombe, M.; Gill, P. M. W.; Johnson, B.; Chen, W.; Wong, M. W.; Gonzalez, C.; and Pople, J. A. *Gaussian, Inc.*, Wallingford CT, 2004.
- (56) (a) Volkov, A.; Li, X.; Koritsanszky, T. S.; Coppens, P. *J. Phys. Chem.* **2004**, *A108*, 4283–4300. (b) Dominiak, P. M.; Volkov, A.; Li, X.; Messerschmidt, M.; Coppens, P. *J. Chem. Theory Comput.* **2007**, *3*, 232–247. Also see the atomic charges from aspherical atom databank at <http://harker.chem.buffalo.edu/group/databank.htm>
- (57) Spackman, M. A.; Munshi, P.; Dittrich, B. *ChemPhysChem.* **2007**, *8*, 2051–2063.
- (58) Spackman, M. A.; Munshi, P.; Jayatilaka, D. *Chem. Phys. Lett.* **2007**, *443*, 87–91.
- (59) Zarychta, B.; Pichon-Pesme, V.; Guillot, B.; Lecomte, C.; Jelsch, C. *Acta Crystallogr.* **2007**, *A63*, 108–125.